

## Research



**Cite this article:** Wang J, Wainwright DK, Lindengren RE, Lauder GV, Dong H. 2020 Tuna locomotion: a computational hydrodynamic analysis of finlet function. *J. R. Soc. Interface* **17**: 20190590.  
<http://dx.doi.org/10.1098/rsif.2019.0590>

Received: 22 August 2019

Accepted: 19 March 2020

**Subject Category:**

Life Sciences—Engineering interface

**Subject Areas:**

biomechanics, biomimetics, biophysics

**Keywords:**

finlets, tuna, swimming, hydrodynamics,

fin–fin interaction, drag reduction

**Author for correspondence:**

Haibo Dong

e-mail: [haibo.dong@virginia.edu](mailto:haibo.dong@virginia.edu)

Electronic supplementary material is available online at <https://doi.org/10.6084/m9.figshare.c.4915584>.

# Tuna locomotion: a computational hydrodynamic analysis of finlet function

Junshi Wang<sup>1</sup>, Dylan K. Wainwright<sup>2</sup>, Royce E. Lindengren<sup>1</sup>, George V. Lauder<sup>2</sup> and Haibo Dong<sup>1</sup>

<sup>1</sup>Department of Mechanical and Aerospace Engineering, University of Virginia, Charlottesville, VA 22904, USA

<sup>2</sup>Museum of Comparative Zoology and Department of Organismic and Evolutionary Biology, Harvard University, Cambridge, MA 02138, USA

JW, 0000-0002-7486-3410; DKW, 0000-0003-4964-5048; HD, 0000-0001-7823-7014

Finlets are a series of small non-retractable fins common to scombrid fishes (mackerels, bonitos and tunas), which are known for their high swimming speed. It is hypothesized that these small fins could potentially affect propulsive performance. Here, we combine experimental and computational approaches to investigate the hydrodynamics of finlets in yellowfin tuna (*Thunnus albacares*) during steady swimming. High-speed videos were obtained to provide kinematic data on the *in vivo* motion of finlets. High-fidelity simulations were then carried out to examine the hydrodynamic performance and vortex dynamics of a biologically realistic multiple-finlet model with reconstructed kinematics. It was found that finlets undergo both heaving and pitching motion and are delayed in phase from anterior to posterior along the body. Simulation results show that finlets were drag producing and did not produce thrust. The interactions among finlets helped reduce total finlet drag by 21.5%. Pitching motions of finlets helped reduce the power consumed by finlets during swimming by 20.8% compared with non-pitching finlets. Moreover, the pitching finlets created constructive forces to facilitate posterior body flapping. Wake dynamics analysis revealed a unique vortex tube matrix structure and cross-flow streams redirected by the pitching finlets, which supports their hydrodynamic function in scombrid fishes. Limitations on modelling and the generality of results are also discussed.

## 1. Introduction

Finlets are commonly found on scombrid fishes (mackerels, bonitos and tunas), which are known for their high swimming speed [1,2] and long-distance swimming ability [3]. Finlets are a series of small, non-retractable fins located at the dorsal and ventral margins of the posterior body of scombrid fishes. Finlet placement is mirrored on the dorsal and ventral sides, and each finlet can move independently with its own pitching kinematics [4,5]. Although individual finlets are small, the summed area of the finlets of a mackerel can reach 15% of its caudal fin area [4–6]. In addition, finlets are located immediately upstream of the caudal fin (the main propulsor of the fish), which suggests that they may play an important role in the swimming dynamics of scombrid fishes.

A number of hypotheses regarding the hydrodynamic effects of finlets have been proposed, and these have mainly focused on possible flow control functions of finlets. One proposal suggested that finlets can redirect the transverse flow across the posterior body of fish to a longitudinal direction, thereby preventing the separation of the boundary layer and thus reducing drag [3,7,8]. Another hypothesis states that finlets can modulate crossflow over the posterior body like ‘flow fences’ [9]. A similar hypothesis indicates that by interfering with vortices shed from the median dorsal and anal fins, finlets can control turbulence at the caudal peduncle [10] and provide a less turbulent flow environment for the caudal fin [11,12]. However, experimental data that address these hypotheses have been challenging to acquire.

Nauen & Lauder [4] first quantified the morphology and kinematics of the chub mackerel (*Scomber japonicus*) finlets and proposed that they may help enhance the thrust generation at the caudal fin by directing flow longitudinally into the caudal fin vortex. Flow visualization data around the finlets and caudal peduncle of chub mackerel [6] were then obtained to confirm the existence of redirected flow across the posterior body caused by the finlets. They also found that the posterior-most finlet contributed to the local flow formation upstream to the caudal fin [6], which may provide favourable flow conditions for tail propulsion. However, it was not possible to obtain detailed flow information such as three-dimensional wake structures for each finlet and potential hydrodynamic interactions among finlets owing to technical limitations of the experiment. Moreover, previous research has not provided any hydrodynamic performance data such as drag/thrust, lateral forces and power consumption for both individual finlets and the assembly of all finlets functioning together during locomotion. Hence it is still unknown if finlets are capable of producing thrust, or if they experience net drag.

A few previous numerical studies [13–15] on the hydrodynamics of simplified finlets have been conducted in fish-like propulsion, in which finlets were modelled as rigid strip-like elongated fins that were not independently mobile. Similar elongated dorsal/anal fins were studied in crevalle jack (*Caranx hippos*) swimming [16]. Among these results, finlets/fins were found to operate in the local flow that is converging to the posterior body, mainly induced by the posteriorly narrowed body of the fishes [14,16]. Enhanced mean thrust and propulsive efficiency attributed to the simplified finlets were found in a tuna-like model [13,15]. Deflected flow across the caudal peduncle by the simplified finlets was also found [14], but the longitudinal flow was not affected [14]. These findings using simplified finlets are in general agreement with the flow visualization data provided by Nauen & Lauder [6], and they partially support earlier hypotheses [3,7,8]. However, the simplified finlet models previously used were continuous fins rather than individually pitching finlets as in swimming scombrid fish. More complex and scombrid-like finlet models will be able to account for the potentially important hydrodynamic effects of finlet–finlet interactions and pitching kinematics.

Therefore, a key general goal of this paper is to study the flow past scombrid fish finlets with biologically realistic geometric and kinematic complexity. In this work, we have conducted a combined experimental and numerical study on the hydrodynamics of tuna finlets during forward swimming. High-speed video of the motion of finlets in freely swimming yellowfin tuna (*Thunnus albacares*) were obtained to provide kinematic data on the *in vivo* motion of finlets. A biologically realistic model of finlets was reconstructed based on measurements of finlets in yellowfin tuna specimens and the kinematics of live fish during free forward swimming. Simulations of the flow past the model finlets were then conducted using a high-fidelity flow solver. By providing detailed flow-field information and hydrodynamic performance data, we aim to extend previous experimental and computational research and fill the gap between numerical studies using simplified finlet models [13–15] and previous experimental work [4,6]. Moreover, we are able to compute the effect of finlet–finlet interaction (FFI) and the effect of pitching kinematics on the wake structure and

hydrodynamic performance of finlets, and we compare the function of individual finlets with an assembled collective array of finlets present in tuna.

## 2. Material and methods

### 2.1. Tuna kinematics and finlet morphology

Swimming kinematics of yellowfin tuna (*T. albacares*) were obtained at the Greenfins tuna facility (Narragansett, RI, USA) where tuna averaging 1 m in fork-length swim freely at approximately 1 body length per second (approx.  $1.0\text{--}1.2\text{ m s}^{-1}$ ) in a 12.2 m diameter tank containing 473 000 l of salt water [17]. This tank is approximately 3 m deep and thus tuna are effectively unconstrained in their locomotion and free to change direction and manoeuvre (figure 1a). Video sequences were obtained with both a Photron Fastcam<sup>®</sup> high-speed camera (250–500 fps, at  $1024 \times 1024$  pixel resolution; Photron USA, Inc.) and a GoPro<sup>®</sup> camera (GoPro, Inc.) mounted above the tank, and another GoPro camera against the tank wall. Videos provided both an overview of body and tail kinematics, and a dorsal view of the dorsal finlets located between the second dorsal fin and the tail. Yellowfin tuna have nine dorsal (A to I, figure 1a) and nine ventral finlets in the caudal peduncle region [18] (figure 1b), but detailed kinematics of the first two and last two were difficult to visualize in freely swimming tuna. Thus, we focus here on finlets three to seven, which we label C to G (figure 1a). Previous research has documented that finlets can be activated by up to three pairs of specialized muscles on each side, which allows scombrid fishes to actively move finlets [4,5] (figure 1c), and active motion does not always result in symmetrical side-to-side finlet amplitude. We frequently observed finlet oscillatory motion with slight right–left asymmetry, and tuna are able to actively move finlets to one side of the body during manoeuvres [17] (not studied here). For the purposes of this computational investigation, we used kinematics from the dorsal finlets only to study their effect on locomotor dynamics.

Anatomical studies of tuna finlets were undertaken to confirm muscular attachments indicated in previous research on mackerel [4] and to quantify the shape of yellowfin tuna finlets. We used photography to document finlet shape and surface area (figure 1d,e), and micro-CT scans of finlet internal skeletal and muscular anatomy [17]. Figure 1f shows the shape of a tuna finlet overlapped by the computational finlet model used in this study. Here,  $s$  denotes the span length of a finlet. The chord length  $c$  is defined at midspan.  $c_{\max}$  denotes the longest chord measured at the finlet root.  $c$  was chosen as the reference length for the hydrodynamic analysis later in this study.

We captured 17 top-view videos of the bodies of different tuna during forward swimming, among which significant finlet kinematics were observed in 12 videos. Figure 2 presents sample image sequences during a complete tail beat cycle ( $T$ ) of one individual tuna in free forward swimming with an approximately constant speed  $U_{\infty}$  at 28.4 chord lengths per tail beat cycle ( $c/T$ ). Nine finlets, from A to I, are labelled. Significant changes in finlet orientations with respect to the body midline were observed during swimming. Among the nine total finlets present, we were able to reconstruct the kinematics of five consecutive finlets beginning with finlet C with the greatest accuracy, and hence focus on these five which we label C to G, as shown in frame  $t/T = 2/11$ . The five finlets are highlighted in yellow and assigned with numeric indices from the first (1st) to the fifth (5th). Finlet roots are highlighted with red dots. The body midline is shown as white dashed line segments that each connect the roots of two consecutive finlets. Finlet angle  $\theta$  defines the pitching motion of a finlet with respect to the body midline. The effective flow velocity  $U_{\text{eff}}$  at a finlet root was estimated as the superposition of swimming velocity  $U_{\infty}$  and root velocity  $U_{\text{root}}$ . The effective angle of

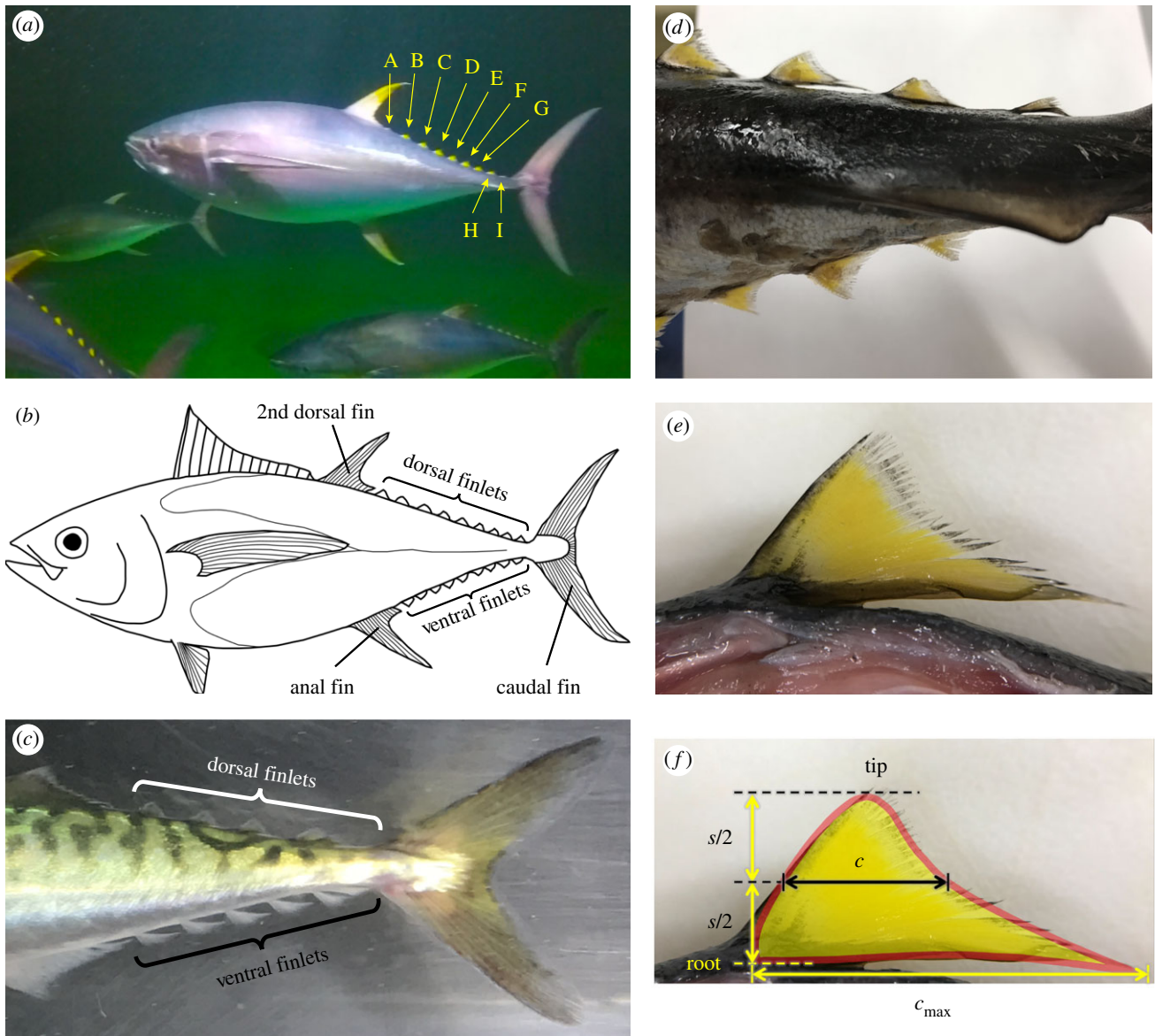


**Figure 1.** (a) Live yellowfin tuna (*Thunnus albacares*) swimming (with nine finlets indicated by letters A to I). (b) Illustration of the dorsal and ventral finlets of a yellowfin tuna. (c) Dorsal and ventral finlets of a mackerel during free swimming. (d) Caudal peduncle region of a yellowfin tuna with finlets. (e) A single tuna finlet to show the attached base and free posterior region. (f) Tuna finlet overlapped by the computational finlet model (red outline).

attack  $\alpha_{\text{eff}}$  was defined as the angle between effective velocity  $U_{\text{eff}}$  and finlet orientation, which serves as an important indicator of the hydrodynamic performance of finlets.

From the 17 top-view videos, we obtained the ranges of the key parameters of tuna steady swimming and finlet kinematics, including the tuna fork-length  $L_B$ , swimming speed  $U_\infty$ , tail beat frequency  $f$ , normalized speed  $U_\infty/fL_B$  and peak-to-peak pitching amplitude  $H_\theta$  of five finlets (table 1). We found that the parameter values from the video chosen for reconstructing finlet kinematics fall well within the range of experimental observations.

In this paper, an image-guided reconstruction method [19] was adopted to reconstruct the finlet kinematics of the yellowfin tuna in Autodesk Maya® (Autodesk, Inc.). This method has been successfully adopted to reconstruct manta ray [20] and fish [16] swimming (see our previous work [16] for more details). The geometric shape shown in figure 1f was scaled to match the actual sizes of the tuna finlets in the video during reconstruction.

The reconstructed finlet model and associated kinematics quantifications are presented in figure 3. Finlet motions during the left-to-right (L-to-R) stroke and right-to-left (R-to-L) stroke, respectively, are shown every  $T/24$  (figure 3a) associated with the side view of the finlet model and the top view of the finlet kinematics in a local coordinate system O-XYZ (figure 3b). The

figure-of-eight shapes denote the root trajectories of the finlets. The arrows represent the longest chords of finlets. Noticeable asymmetry in finlet angles was observed between the L-to-R and the R-to-L strokes, and this was commonly observed during finlet motion in swimming tuna [17]. The normalized geometric quantities of the finlet model are marked in figure 3b and listed in table 2. Here,  $A$  denotes the peak-to-peak amplitude of the finlet root.  $L$  denotes the total length of the assembly of finlets when the posterior body is stretched and no finlet kinematics are applied, and  $L$  is  $10.1c$ . All lengths are normalized by the chord length  $c$  of the first finlet, and the finlet area  $S$  is normalized by  $c^2$ .

It was found that the peak-to-peak values of the normalized instantaneous lateral root displacement ( $z/c$ ), finlet angle ( $\theta$ ) and geometric angle of attack ( $\alpha$ ) all increased posteriorly from the first finlet to the fifth finlet (figure 3c–e). The phase difference in the peaks of  $z/c$ ,  $\theta$  and  $\alpha$ , in general, increased posteriorly. Through the maximum, minimum and mean values of the finlet angle in figure 3f, we found that the asymmetry in  $\theta$  alleviated posteriorly with mean angle decreased from  $20.9^\circ$  at the first finlet to  $6.4^\circ$  at the fifth finlet. An analytical representation of finlet model kinematics is provided in the electronic supplementary material.

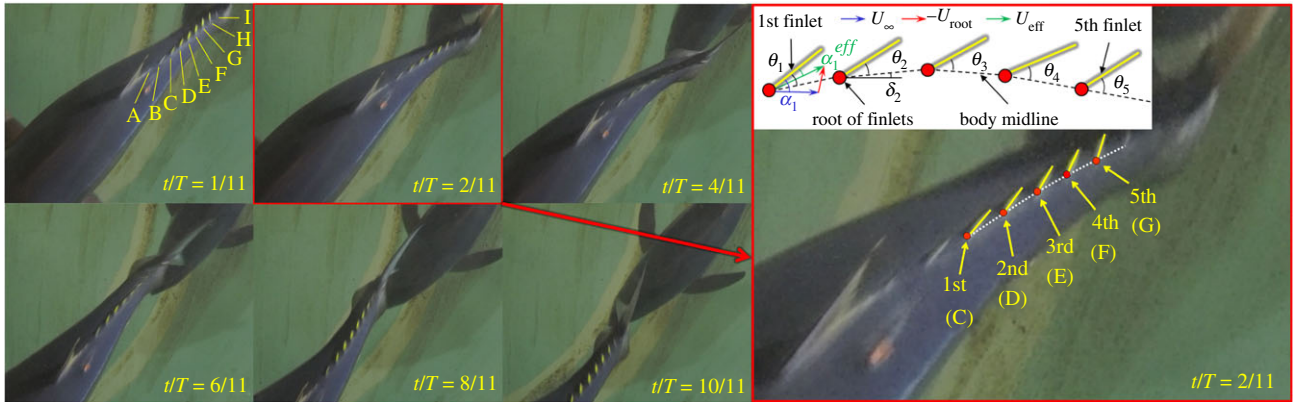


**Figure 2.** Top-view snapshots of a yellowfin tuna (*Thunnus albacares*) in forward swimming during one tail beat cycle. Nine finlets (A to I) are labelled in the upper left panel, but only the function of five (C to G) were analysed in detail here. Body midline angle ( $\delta$ ) defines the angle between the body midline and the body sagittal plane. The geometric angle of attack ( $\alpha$ ) is the angle between the finlet and the body sagittal plane. Finlet angle ( $\theta$ ), effective angle of attack ( $\alpha_{\text{eff}}$ ), effective velocity ( $U_{\text{eff}}$ ), swimming velocity ( $U_{\infty}$ ) and the instantaneous root velocity of the finlet ( $U_{\text{root}}$ ) are also shown.

**Table 1.** Summary of key parameters of tuna steady swimming and finlet kinematics.

	fork-length, $L_B$ (m)	swimming speed, $U_{\infty}$ ( $\text{m s}^{-1}$ )	tail beat frequency, $f$ (Hz)	normalized speed, $U_{\infty}/fl_B$	peak-to-peak pitching amplitude, $H_{\theta}$ (deg.)				
					first finlet	second finlet	third finlet	fourth finlet	fifth finlet
observed range	0.8–1.2	1.0–1.2	2.3–3.4	0.25–0.46	20–35	40–55	45–60	70–90	80–120
present kinematics	1.0	1.0	2.8	0.36	28	52	54	81	109

## 2.2. Numerical method and simulation set-up

The governing equations of the flow past finlets solved in this paper are the incompressible Navier–Stokes equations, written in indicial form as

$$\frac{\partial u_i}{\partial x_i} = 0; \quad \frac{\partial u_i}{\partial t} + \frac{\partial u_i u_j}{\partial x_j} = -\frac{\partial p}{\partial x_i} + \frac{1}{Re} \frac{\partial^2 u_i}{\partial x_j \partial x_j}, \quad (2.1)$$

where  $u_i$  are the velocity components,  $p$  is the pressure and  $Re$  is the Reynolds number.

The equations are solved using a Cartesian-grid-based sharp-interface immersed-boundary method [21], which has been successfully applied to simulate biological flapping propulsions including fish [16] and manta ray [22] swimming. More details of the flow solver are provided in the electronic supplementary material.

A Cartesian computational grid with stretching grid configuration was employed in the simulations (figure 4a). The computational domain size was  $40c \times 16c \times 20c$  with total grid points around 9.0 million ( $385 \times 81 \times 289$ ) and a minimum grid spacing at  $\Delta_{\text{min}} = 0.029c$ . The grid was designed to resolve the fluid field in the vicinity of the computational model and its wake with high resolution. The left-hand boundary was set as the velocity inlet with constant incoming flow speed  $U_{\infty}$ . A homogeneous Neumann boundary condition was used for the pressure at all boundaries. A no-slip boundary condition was applied at the model surface. Previous numerical results of tuna [13,14,23,24] and jackfish [16] swimming and recent experimental flow visualization of robotic tuna models [25,26] both show that the local flow past the posterior bodies of the fishes/model was converging to the posteriorly narrowed bodies. Therefore, the incoming flow  $U_{\infty}$  in this paper was set to be parallel to the stroke plane of finlets to mimic the local flow condition of finlets as in tuna swimming. We do not include the effect of the body and caudal fin of tuna in these simulations so that finlet flows can be studied in isolation, although in the electronic supplementary material we provide additional computational

results that illustrate the effect of the body on finlet flow, and the effect of finlet flow patterns on the function of the caudal fin. More details on the validation of the uniform incoming flow assumption are provided in the electronic supplementary material.

We used extensive simulation tests to prove that the size of the computational domain was large enough to obtain convergent results. In addition, a convergence study was performed to demonstrate the grid-independent results. Figure 4b shows the comparison of the instantaneous drag coefficient of the isolated first finlet at four different grid densities. The minimum grid spacings of the coarse, medium, fine and dense meshes are  $0.088c$ ,  $0.044c$ ,  $0.029c$  and  $0.016c$ , respectively. The drag coefficient converged as the grid spacing decreased. The mean drag difference between the fine and the dense mesh was less than 3.0%.

In this study, the key parameters associated with the flow simulation of finlets are the Reynolds number  $Re$  and the reduced frequency  $k$  defined as follows, respectively:

$$Re = \frac{U_{\infty} c}{\nu} \quad \text{and} \quad k = \frac{fA}{U_{\infty}}, \quad (2.2)$$

where  $U_{\infty}$  is the incoming flow pointing to  $x$ -positive,  $c$  is the chord length of the first finlet,  $\nu$  denotes the kinematic viscosity,  $f$  is the tail beat frequency and  $A$  is the peak-to-peak root amplitude of the fifth finlet.

In this paper, the measured  $k$  of finlets during living tuna swimming was around 0.206, and the measured  $Re$  of the first finlet was around  $1.0 \times 10^4$ . The corresponding  $Re$  of the yellowfin tuna was approximately  $1.0 \times 10^6$ , which is challenging for direct numerical simulations. The purpose of conducting viscous flow simulation is to characterize the fundamental flow features of finlets. Previous studies have shown that key wake structure features in the propulsion of flapping foils [27] and fish pectoral fin [28] swimming are robust to changing  $Re$ . Zhong *et al.* [26] simulated a model fish swimming at  $Re = 2100$ , and the wake patterns obtained from the simulation showed strong similarities to

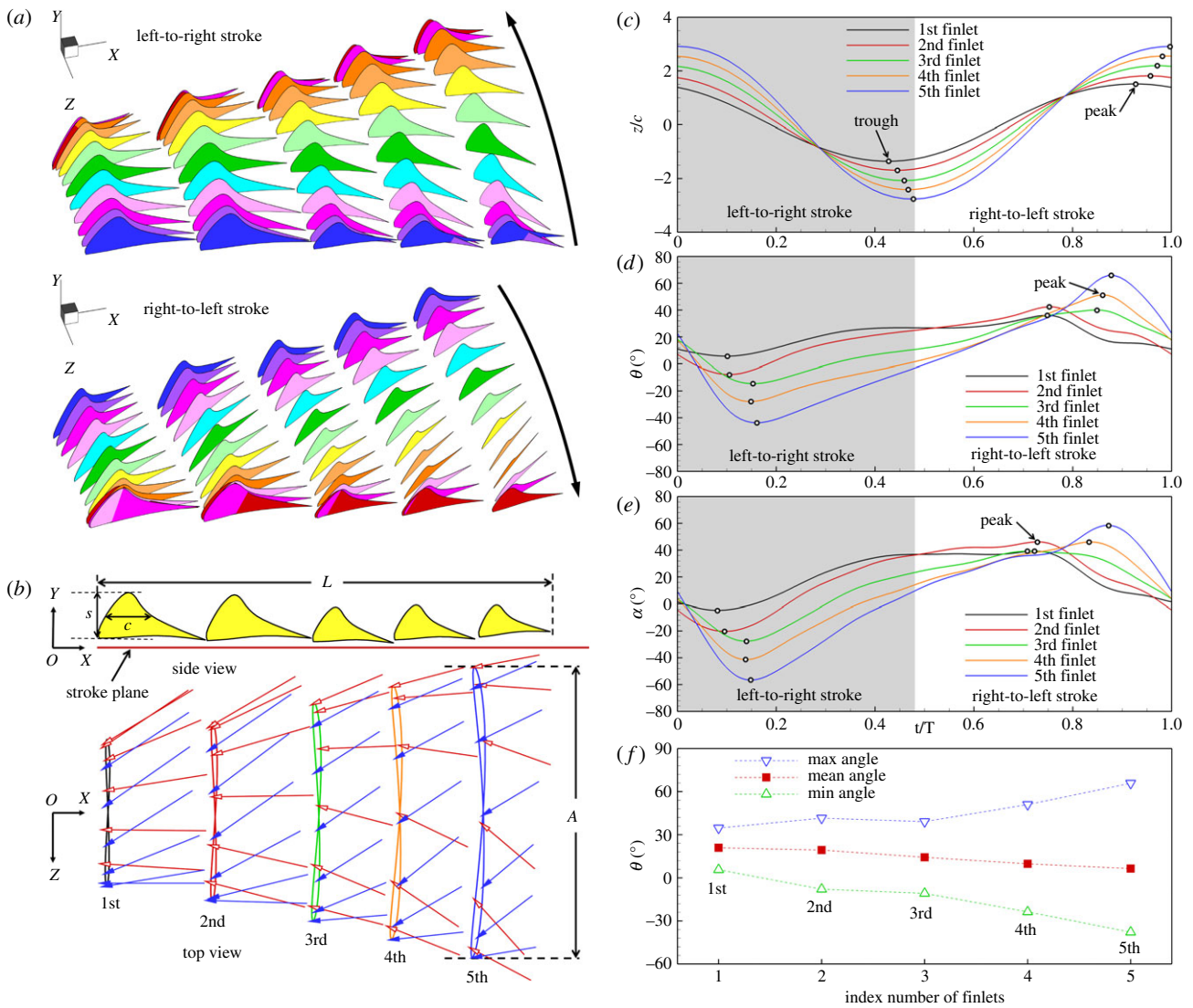


**Figure 3.** Reconstructed finlet motion during the left-to-right stroke and the right-to-left stroke, respectively, from a perspective view (a) and top view (b). In (a), a change in finlet colour corresponds to a change in time of  $T/24$ . The instantaneous lateral root displacement ( $z/c$ ), finlet angle ( $\theta$ ) and geometric angle of attack ( $\alpha$ ) of the five finlets during one tail beat cycle are plotted in (c–e), respectively. The maximum, minimum and mean values of each finlet angle are shown in (f).

**Table 2.** Normalized geometric quantities of the reconstructed finlet model.

reconstructed model	chord length, $c$	max chord length, $c_{\max}$	span length, $s$	finlet area, $S$	root amplitude, $A$
first finlet	1.00	2.31	1.01	1.02	2.86
second finlet	0.98	2.26	0.99	0.97	3.50
third finlet	0.76	1.75	0.77	0.59	4.28
fourth finlet	0.75	1.73	0.76	0.57	4.97
fifth finlet	0.67	1.54	0.67	0.45	5.85

their experimental results using the same model but conducted at  $Re$  values 20–50 times higher. There are also other precedents in simulating fish swimming [16,20,29] that reduce the  $Re$  to the order of  $10^3$  or lower to study the fundamental flow mechanisms at a feasible computational cost. In this paper, in order to understand the vortex dynamics, the finlets were simulated at  $Re$  of the order of  $10^3$  to meet the requirements of both accuracy and computational cost. A validation study on the  $Re$  used for the present simulations is provided in the electronic supplementary material.

In this paper, the simulations were conducted at  $Re = 999.6$  and  $k = 0.206$ . The results presented, including the hydrodynamic performance and wake topology of the reconstructed finlet

model, are from the fifth tail beat cycle of the simulations when the flow field has reached a periodic state. The effect of FFI is investigated by comparing the results of the array of all five finlets with results from a single isolated finlet. In addition, the effect of pitching kinematics of finlets is studied by comparing the results of finlet motion with (w/) and without (w/o) pitching. A list of the computational cases conducted is provided in the electronic supplementary material.

The hydrodynamic force acting on finlets is computed by the direct integration of instantaneous pressure and shear over the finlet surface. The hydrodynamic power output is defined as the rate of instantaneous work done by the finlet. The drag ( $F_x$ ),

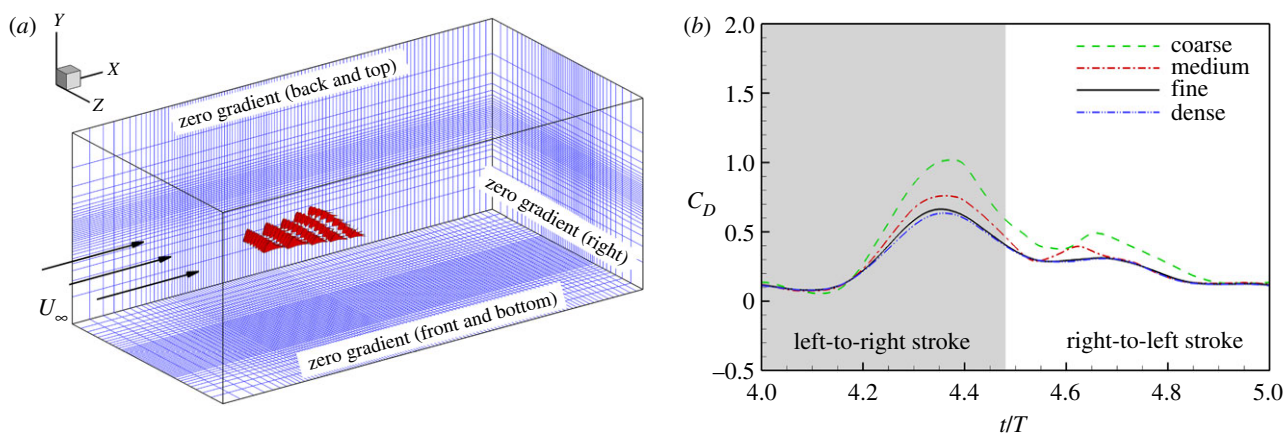


**Figure 4.** (a) Schematic of the computational mesh and boundary conditions used in the present simulation, where  $U_\infty$  denotes incoming flow speed. (b) Comparison of the instantaneous drag coefficient of the isolated first finlet between coarse, medium, fine and dense mesh. In (a), five finlets are shown at 24 different times throughout the tail beat cycle.

lateral ( $F_z$ ) forces and power output ( $P_{\text{out}}$ ) are non-dimensionalized as drag ( $C_D$ ), lateral ( $C_Z$ ) and power ( $C_{\text{PW}}$ ) coefficients, respectively, as shown below

$$C_D = \frac{F_x}{(1/2)\rho U_\infty^2 S} \quad C_Z = \frac{F_z}{(1/2)\rho U_\infty^2 S} \quad C_{\text{PW}} = \frac{P_{\text{out}}}{(1/2)\rho U_\infty^3 S}, \quad (2.3)$$

where  $F_x$  points to  $x$ -positive,  $F_z$  points to  $z$ -positive,  $\rho$  is fluid density,  $S$  denotes the area of the first finlet and  $U_\infty$  is the incoming flow speed at 28.4 chord lengths per tail beat cycle.

### 3. Results

We first present the hydrodynamics performance and wake topology of the five reconstructed finlets together in §3.1. We found all finlets were drag producing. Vortex dynamics analysis revealed a unique vortex matrix consisting of counter-rotating vortex tube pairs. The hydrodynamic effect of FFI was then studied in §3.2. It was found the total drag of the finlets array was reduced by 21.5% due to flow interactions between finlets. The effect of pitching kinematics of finlets was studied in §3.3. Significant mean lateral forces were produced due to finlets pitching, which could help tuna to manoeuvre by generating yaw torques. Pitching kinematics also helped reduce the total power consumption by 20.8% and generate a constructive force to facilitate posterior body flapping. In addition, clear flow channels between pitching finlets were found, which supports several aspects of previous hypotheses on finlet function.

#### 3.1. Hydrodynamic performance and wake topology of finlets

The instantaneous drag and lateral force coefficients of the array of five finlets (figure 5a,b) both show two major peaks associated with the unsteady flapping motions of finlets near the midstroke of L-to-R and R-to-L strokes, respectively. Forces produced by finlets show a strong correlation with the effective angle of attack  $\alpha_{\text{eff}}$  (figure 5c). In general, larger  $\alpha_{\text{eff}}$  corresponds to larger drag and lateral force generations. Owing to the asymmetry in finlet angle ( $\theta$ ), both forces show noticeable asymmetric behaviour between the two strokes.

We found that all finlets were drag producing during forward swimming and that no thrust was generated (figure 5a), which is in line with the conclusion of drag-producing mackerel finlets [6]. The first finlet (finlet C, figure 2) produced the

most drag among all finlets, followed by the second finlet (finlet D). Large positive lateral forces were produced at the first and second finlets during L-to-R stroke (figure 5b). More posterior finlets had more symmetric behaviour in lateral force between two strokes, which is in line with the behaviour of the finlet angle (figure 2d).

The cycle-averaged drag ( $\bar{C}_D$ ) and lateral force coefficients ( $\bar{C}_Z$ ) in table 3 show that the first finlet produced 39.9% of the total  $\bar{C}_D$  and 55.2% of the total  $\bar{C}_Z$ . It was found that  $\bar{C}_Z$  decreased posteriorly, sharing the same trend of mean finlet angle in figure 2f.

Vortex dynamics of finlet flow are analysed in detail during a tail beat cycle (figure 5d(i–vi)). The instantaneous three-dimensional wake structure was visualized using iso-surfaces of the  $Q$ -criterion [30] and flooded by vorticity  $\omega_x$ . Comparing between the two strokes, the most distinctive difference in vortex topology was that the tip vortices (TVs) and root vortices (RVs) merged into one strong counter-rotating vortex pair during the L-to-R stroke (figure 5d(i–iii)), while they remained separated as five vortex pairs during the R-to-L stroke to form a parallel-aligned  $5 \times 2$  vortex tube matrix (figure 5d(iv–vi)).

Specifically, at early L-to-R stroke (i), a pair of counter-rotating vortices, including a TV and an RV, emerged at the tip and root of the first finlet. A shear layer (SL-1) was also observed. At middle L-to-R stroke (ii), significant TVs were developed at the first four finlets (first to fourth) as four vortex tubes (TV-1 to TV-4), and the RVs merged together to form a coherent vortex tube. Meanwhile, the SL-1 has strengthened into a leading-edge vortex (LEV-1), attaching to the leeward of the first finlet. At late L-to-R stroke (iii), the individual TVs also merged into one coherent TV tube, resulting in a pair of parallel and strong counter-rotating vortex tubes (TV and RV).

At early R-to-L stroke (iv), the reversal in finlet motion caused the previously formed TV and RV to shed, and new RVs started to form individually at finlet roots. At middle R-to-L stroke (v), the newly formed TVs and RVs of the first four finlets (first to fourth) developed into four pairs of counter-rotating vortex tubes that elongated parallelly towards downstream. No obvious merge of TVs or RVs was observed. At late R-to-L stroke (vi), the vortex pairs of the first and second finlets shrank, while those of the fourth and fifth finlets intensified. The SL-4 and SL-5 also strengthened and developed into LEVs.

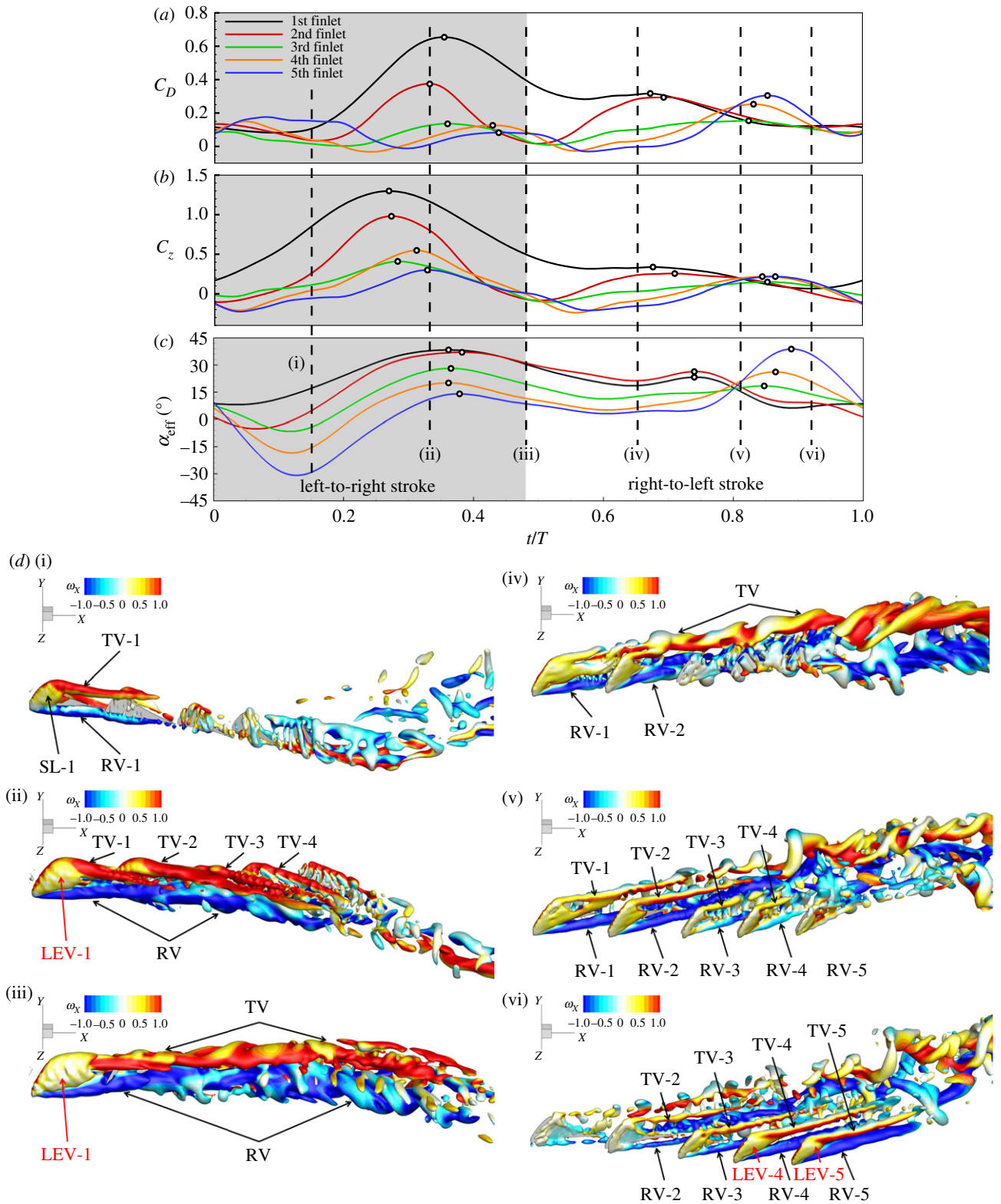


**Figure 5.** Instantaneous drag coefficient (a), lateral force coefficient (b) and effective angle of attack (c) of finlets during one tail beat cycle of tuna forward swimming. (d) Three-dimensional wake structure of finlets at (i)  $t/T = 0.15$ , (ii)  $t/T = 0.33$ , (iii)  $t/T = 0.48$ , (iv)  $t/T = 0.65$ , (v)  $t/T = 0.81$  and (vi)  $t/T = 0.92$ , respectively, from a perspective view. The isosurface of the wake structures is visualized by  $Q = 150$ . The  $Q$ -isosurface is filled by the contour of vorticity  $\omega_x$ , which is normalized by  $U_\infty/c$ . The tip vortex (TV), root vortex (RV), shear layer (SL) and leading-edge vortex (LEV) are identified for each finlet.

**Table 3.** Cycle-averaged drag ( $\bar{C}_D$ ) and lateral force ( $\bar{C}_Z$ ) coefficients of finlets.

index	first finlet	second finlet	third finlet	fourth finlet	fifth finlet	total
$\bar{C}_D$	0.283	0.164	0.083	0.085	0.095	0.710
$\bar{C}_Z$	0.535	0.235	0.106	0.080	0.013	0.969

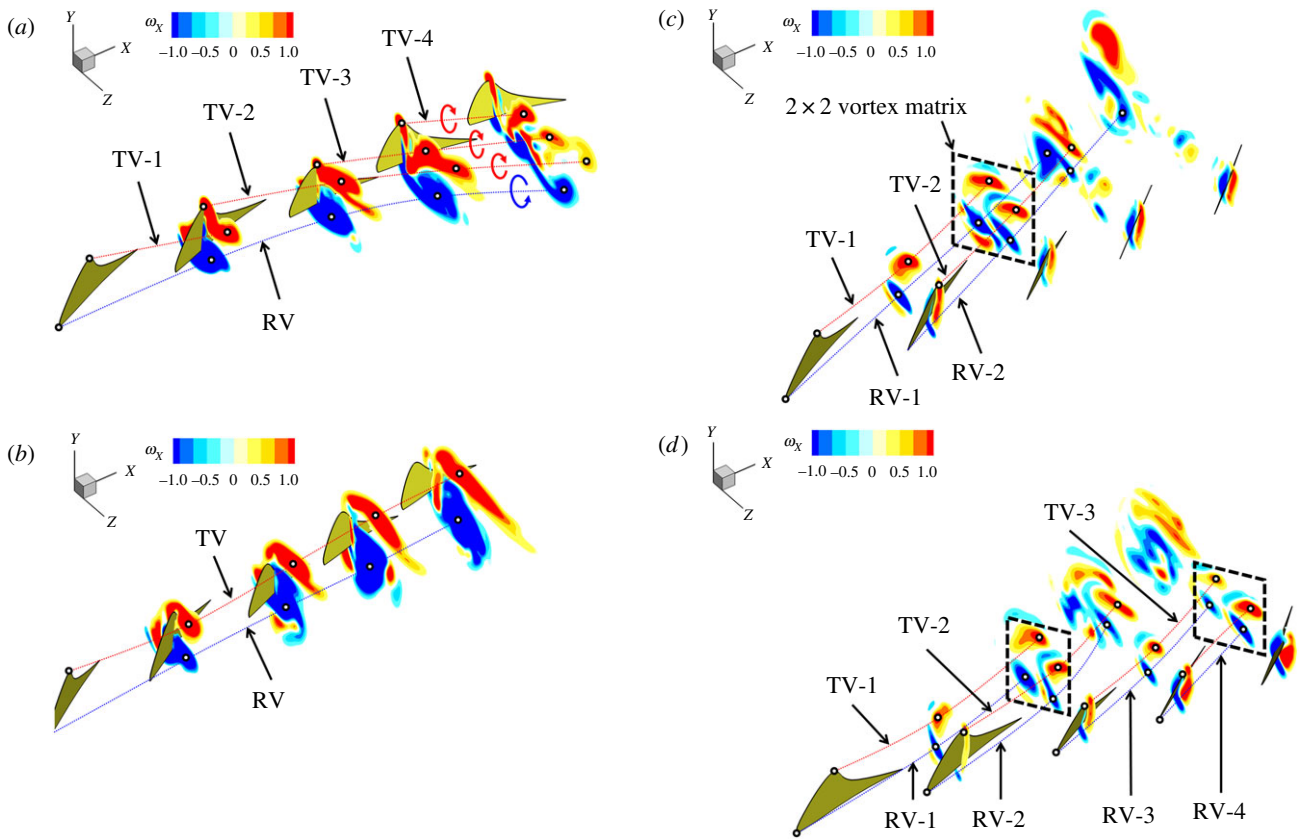


**Figure 6.** Contour of  $\omega_x$  on four vertical slices cutting the second, third, fourth and fifth finlet, respectively, at (a)  $t/T = 0.33$ , (b)  $t/T = 0.48$ , (c)  $t/T = 0.81$  and (d)  $t/T = 0.92$ , from a perspective view.  $\omega_x$  is normalized by  $U_\infty/c$ . The centrelines of root vortices (RVs) and tip vortices (TVs) are illustrated with dotted red and blue lines, respectively, connecting vortex cores (white dots) on each slice. The TV and RV are identified.

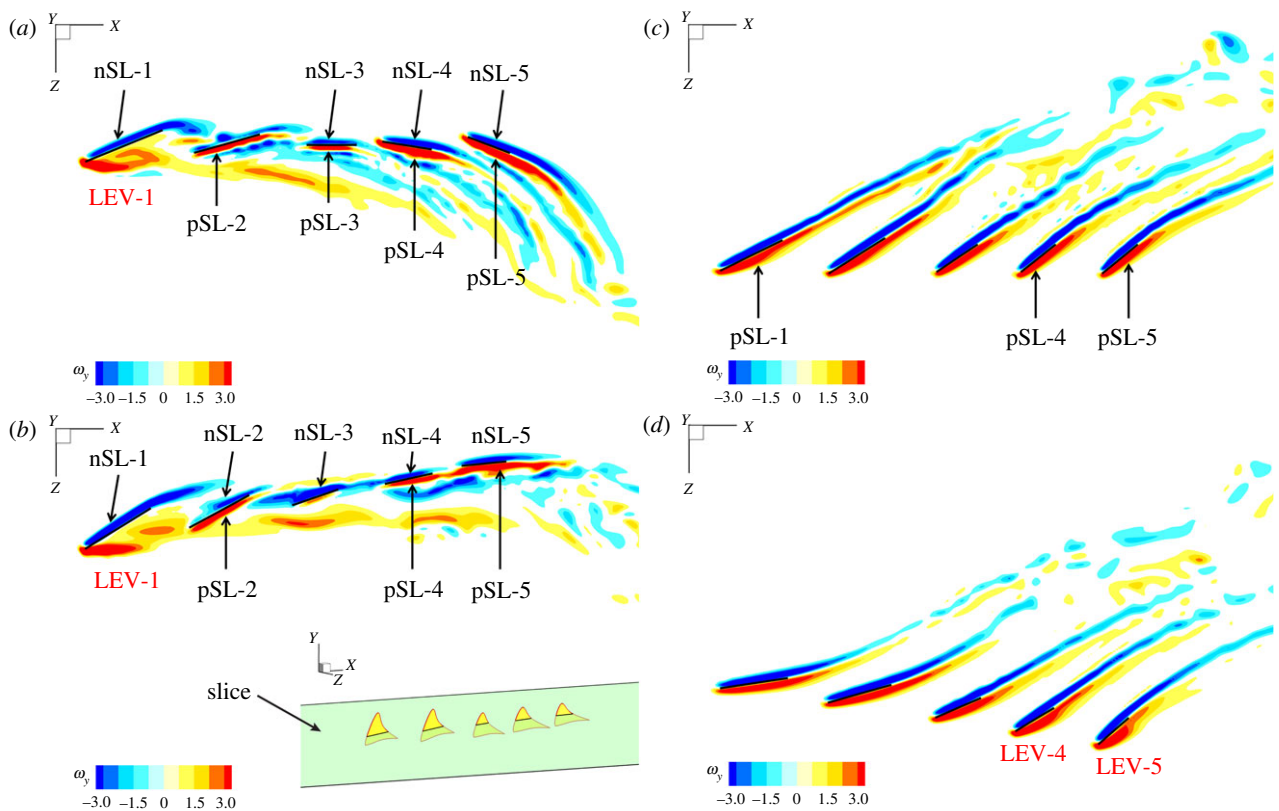


**Figure 7.** Contour of  $\omega_y$  on a horizontal slice cutting through a horizontal slice 0.3 s above the root of the first finlet at (a)  $t/T = 0.33$ , (b)  $t/T = 0.48$ , (c)  $t/T = 0.81$  and (d)  $t/T = 0.92$ , respectively, from top view.  $\omega_y$  is normalized by  $U_\infty/c$ . The negative shear layer (nSL), positive shear layer (pSL) and leading-edge vortex (LEV) are identified for each finlet.

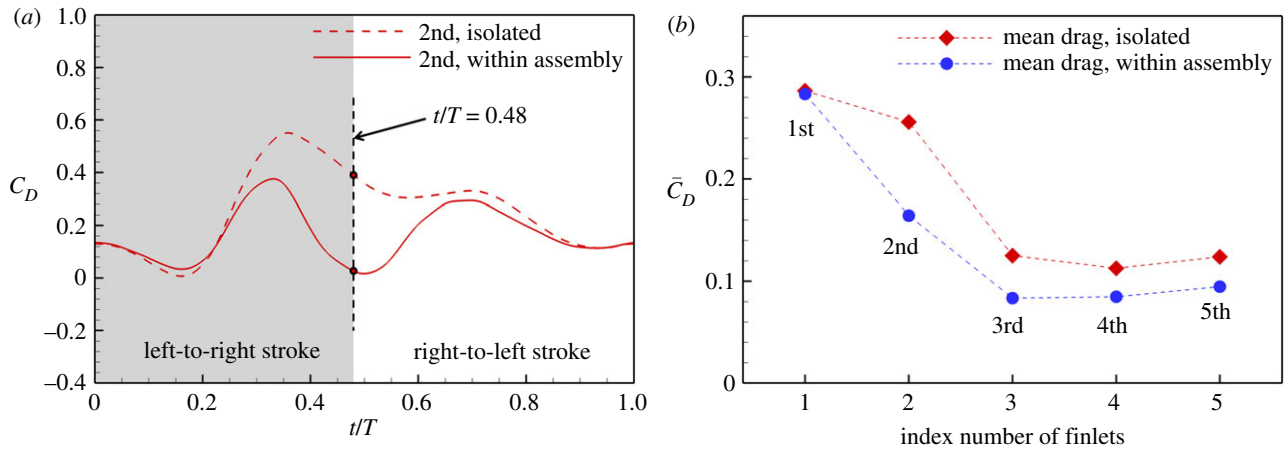


**Figure 8.** (a) Comparison of instantaneous drag coefficient ( $C_D$ ) between the isolated second finlet and the second finlet when located within the assembly of five. (b) Comparison of cycle-averaged drag coefficient ( $\bar{C}_D$ ) between the isolated finlets and their within-assembly counterparts.

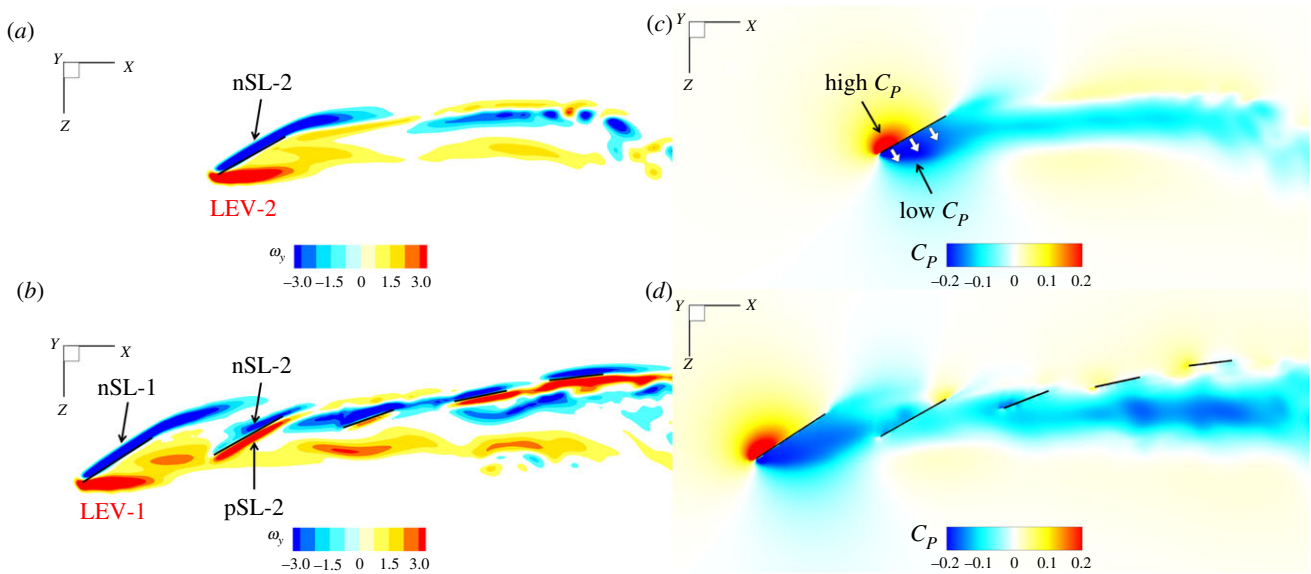


**Figure 9.** Comparisons of the vorticity  $\omega_y$  (a,b) and pressure coefficient  $C_p$  (c,d) contours between the isolated second finlet (a,c) and its in-assembly counterpart (b,d), respectively, at  $t/T=0.48$  on a horizontal slice cutting through a chord of the first finlet. The negative shear layer (nSL), positive shear layer (pSL) and leading-edge vortex (LEV) are identified. In (c), white arrows denote the pressure force.

**Table 4.** Drag reduction due to finlet–finlet interaction.

	first finlet	second finlet	third finlet	fourth finlet	fifth finlet	total
drag reduction, $\Delta\bar{C}_D$ (%)	1.0	35.9	33.6	24.8	23.4	21.5

The wake topology of finlets was further clarified with  $x$ -vorticity contours ( $\omega_x$ ) (figure 6a–d). In general, the vortex structures revealed by vorticity contours are consistent with the  $Q$ -isosurfaces in figure 5d. At middle R-to-L stroke ( $t/T=0.81$ ), the TVs and RVs, corresponding to those shown in figure 5d(v), are clearly identified. Multiple vortices, including TV-1, TV-2, RV-1 and RV-2, were cut simultaneously by the slice on the third finlet. The four vortices formed the unique pattern of a counter-rotating  $2 \times 2$  vortex matrix (dashed black box in figure 6c), with the TV and RV cores clearly separated and parallel aligned. No noticeable interactions were observed among them. At  $t/T=0.92$ , another  $2 \times 2$  vortex matrix was formed containing the wake from the third and fourth finlets. It is noteworthy that the strengths of individual TVs and RVs from R-to-L stroke were much weaker than those from L-to-R stroke, indicating

weaker disturbances of the incoming flow by finlets, which may explain the smaller lateral force generation during the R-to-L stroke (figure 5b).

Shear layers on finlets are visualized by  $y$ -vorticity contour  $\omega_y$  (figure 7a–d). Owing to the asymmetry in pitching kinematics of finlets, the interactions between shear layer and downstream finlets were more significant during the L-to-R stroke than during the R-to-L stroke. At middle L-to-R stroke ( $t/T=0.33$ ), because of the large effective angle of attack of the first finlet ( $\alpha_{\text{eff}}=38.2^\circ$ , figure 5c), an LEV was formed, which explained the large drag and lateral force generations of the first finlet at this moment (ii, figure 5a,b). At  $t/T=0.48$ , the LEV core detached from the finlet, resulting in drops in both the drag and lateral forces (iii, figure 5a,b). At middle R-to-L stroke ( $t/T=0.81$ ), no LEV was formed owing to the low  $\alpha_{\text{eff}}$  at all finlets (approx.  $17^\circ$ , figure 5c).

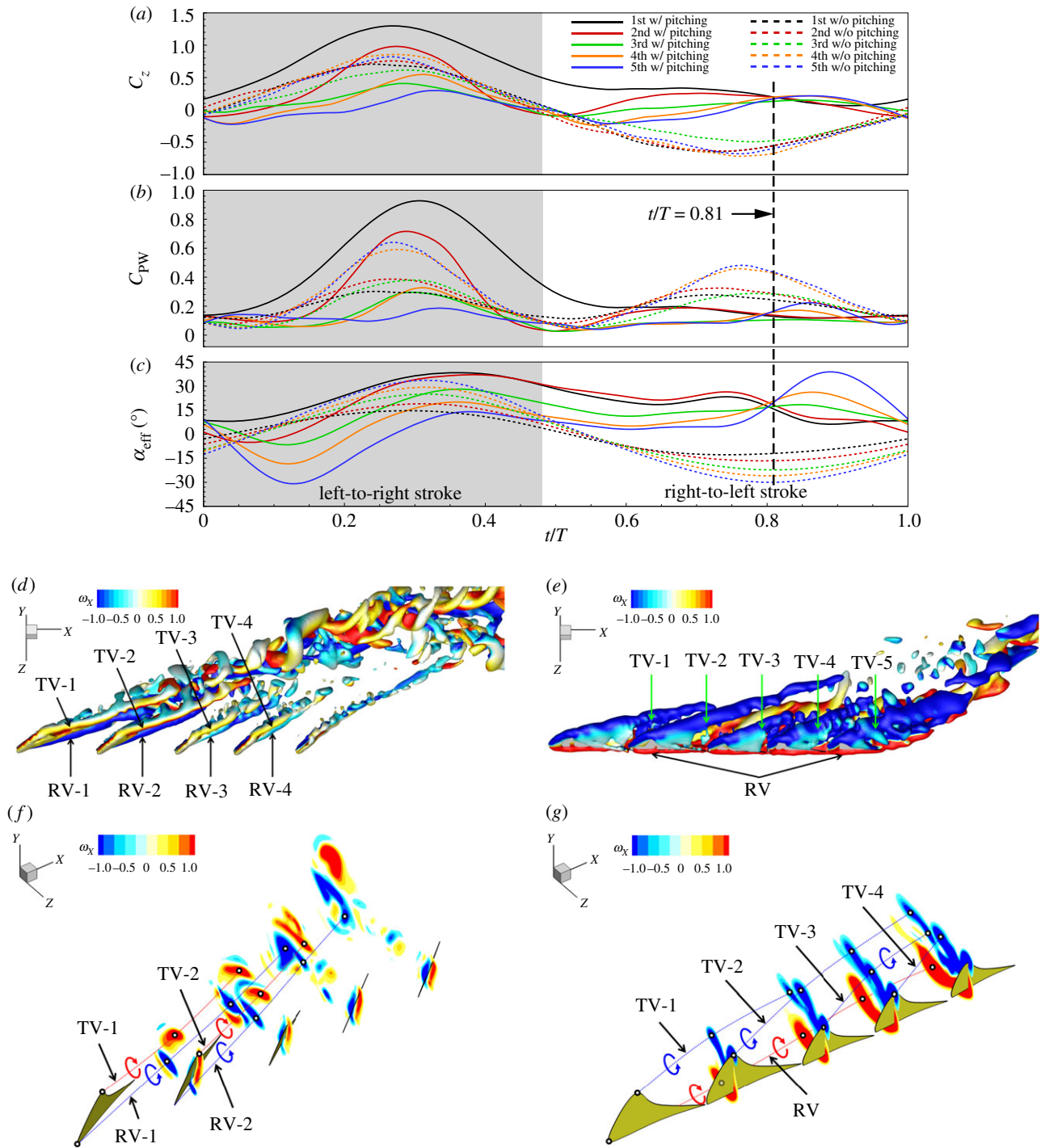


**Figure 10.** Comparisons of the instantaneous lateral force coefficient (a), power coefficient (b), effective angle of attack (c), wake structure (d,e) and  $x$ -vorticity contour (f,g), respectively, between finlets with and without pitching kinematics. The wake structures and  $x$ -vorticity contours are shown at  $t/T = 0.81$ . The tip vortex (TV) and root vortex (RV) are identified for each finlet.

All shear layers were found to be attached to the finlets and elongated towards downstream of local flow to form a parallel wake pattern, which was also observed by the corresponding  $Q$ -isosurfaces in figure 5d(v). At  $t/T = 0.92$ , the shear layer wakes were maintained separated from each other. LEVs start to develop on the fourth and fifth finlets because of their high  $\alpha_{\text{eff}}$  at the moment (vi, figure 5c).

### 3.2. Effects of finlet–finlet interaction

To study the effect of finlet–finlet interactions, we compare the force and flow results between an isolated finlet and the finlet when located within the five-finlet assembly. For the

second finlet, a significant difference in instantaneous drag coefficient ( $C_D$ ) was found during late L-to-R and early R-to-L stroke with the largest discrepancy at  $t/T = 0.48$  (figure 8a). The cycle-averaged drag coefficient ( $\bar{C}_D$ ) of isolated finlets and finlets in-assembly are plotted in figure 8b. A significant drop in  $\bar{C}_D$  was found for the last four finlets (second to fifth), which was caused by hydrodynamic interactions between the finlets, as shown in figure 7a,b.

The individual and total drag reduction of finlets due to FFI are calculated in table 4. The drag reduction ratio ( $\Delta\bar{C}_D$ ) is defined by  $\Delta\bar{C}_D = (\bar{C}_{D|\text{isolated}} - \bar{C}_{D|\text{within assembly}}) / \bar{C}_{D|\text{isolated}}$ . The largest drag reduction happened at the second finlet with a 35.9% drop in drag compared with the isolated

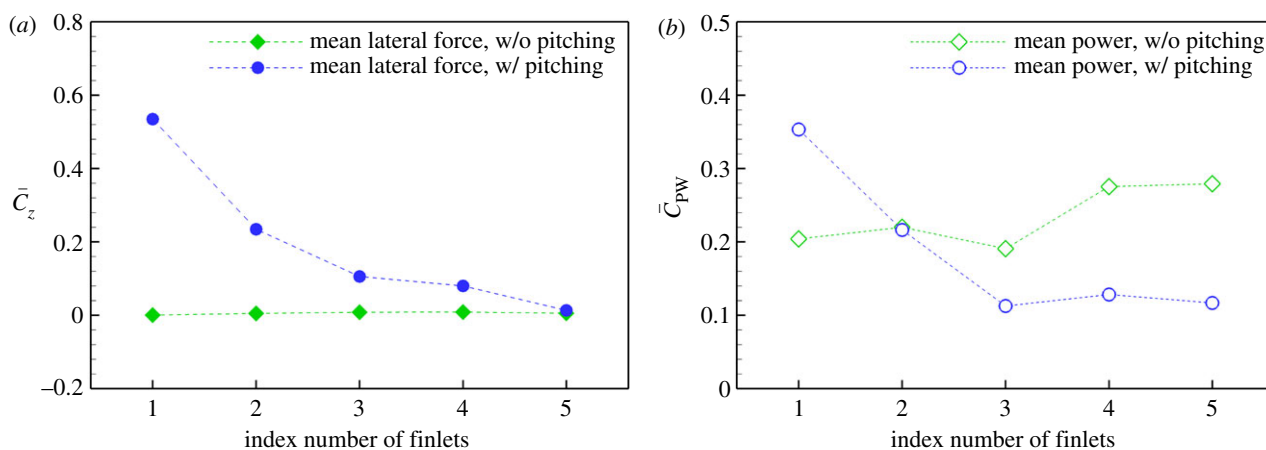


**Figure 11.** Comparisons of the cycle-averaged lateral force (a) and power coefficients (b), respectively, between the finlets with and without pitching kinematics.

**Table 5.** Power reduction due to pitching kinematics of the finlets.

	first finlet	second finlet	third finlet	fourth finlet	fifth finlet	total
power reduction, $\Delta\bar{C}_{PW}$ (%)	-73.0	1.8	40.8	53.6	58.1	20.8

second finlet. The total drag of the assembly of five was 21.5% less than the summed drag of their isolated counterparts.

The fundamental reason for FFI-induced drag reduction is revealed by comparing the wake structure and pressure field between the isolated finlet and the finlet within assembly (figure 9) when the instantaneous drag coefficient on the second finlet has the largest difference (figure 8a). Because the second finlet was located at the lee side of the first finlet, the first finlet was acting as a deflector, which prevented the direct impact of the incoming flow on the second finlet. As a result, the strengths of pSL-2 and nSL-2 within the assembly of five (figure 9b) were much weaker than those of their isolated counterparts (figure 9a). Instead, nSL-1 and LEV-1, which are similar to those of the isolated second finlet in shape and strength, were formed at the first finlet. In addition, the pSL-2 in figure 9b was attached to the finlet, which is different from the detached LEV-2 in figure 9a.

The FFI-induced drag reduction is confirmed by comparing the pressure contour around finlets between the two models (figure 9c,d). A large pressure difference between the two sides of the isolated second finlet was found, which creates a large pressure force normal to the finlet surface with its  $x$ -positive component contributing to drag production. For the second finlet within assembly, because of the deflection effect created by the first finlet, there was no significant pressure difference between the two sides, resulting in a much lower instantaneous drag than that of the isolated second finlet at this moment ( $t/T=0.48$ , figure 8a).

### 3.3. Effect of pitching kinematics of finlets

We investigate the effect of pitching kinematics of finlets by comparing the force and flow between finlets with (w/) and without (w/o) pitching. The finlets w/o pitching were fixed to the body along the local body centreline at all times and thus did not move independently of the body centreline motion pattern. Major differences in the instantaneous lateral forces coefficient ( $C_z$ ) happen between finlets w/ and w/o pitching during the R-to-L stroke when their  $\alpha_{\text{eff}}$  were

opposite in signs (figure 10a,c). In addition, clear flow channels between neighbouring finlets were observed for pitching finlets at  $t/T=0.81$ . By contrast, the body-fixed finlets were consecutively placed in a row with small clearances between each other. Therefore, no channel between finlets was formed (figure 10d-g).

The  $\alpha_{\text{eff}}$  of the body-fixed finlets (figure 10c) were more symmetric between the L-to-R and the R-to-L strokes than that of the pitching finlets, resulting in more symmetric  $C_z$  and power consumption ( $C_{PW}$ ) between the two strokes. For the flow, it was interesting to find that the rotation directions of both the TVs and RVs generated by pitching finlets were opposite to those generated by body-fixed finlets (figure 10f,g), resulting from the opposite signs of  $\alpha_{\text{eff}}$ . In addition, the merged RV of the body-fixed finlets kept in close proximity to the finlets array, while the TVs of pitching finlets were maintained separated and diverged from the finlets (figure 10f,g). Stronger TVs and RVs generated by the body-fixed finlets caused the higher  $\alpha_{\text{eff}}$  (figure 10d,e).

The cycle-averaged lateral force coefficient ( $\bar{C}_z$ ) shows the large mean lateral forces produced by the first and second finlets owing to their asymmetric pitching angles (figure 11a), which accounted for 79% of the total mean lateral force of the five finlets. The lateral force could help fish to manoeuvre by generating yaw torques, which is a potentially beneficial hydrodynamic effect of the pitching kinematics of the finlets. In support of this idea, low-speed manoeuvres in scombrid fishes using only finlets have been observed [6]. Because of the symmetric property of lateral forces for body-fixed finlets, little mean net force was produced (figure 11a).

The cycle-averaged power consumption (figure 11b) in general increased posteriorly for the body-fixed finlets but decreased posteriorly for the pitching finlets. The pitching kinematics of finlets resulted in much smaller mean power at the last three finlets than their body-fixed counterparts.

The pitching-induced power reductions of finlets are calculated and listed in table 5. The power reduction ( $\Delta\bar{C}_{PW}$ ) is defined by  $\Delta\bar{C}_{PW} = (\bar{C}_{PW|w/o} - \bar{C}_{PW|w}) / \bar{C}_{PW|w/o}$ . Over half of the hydrodynamic power of the last two finlets (fourth

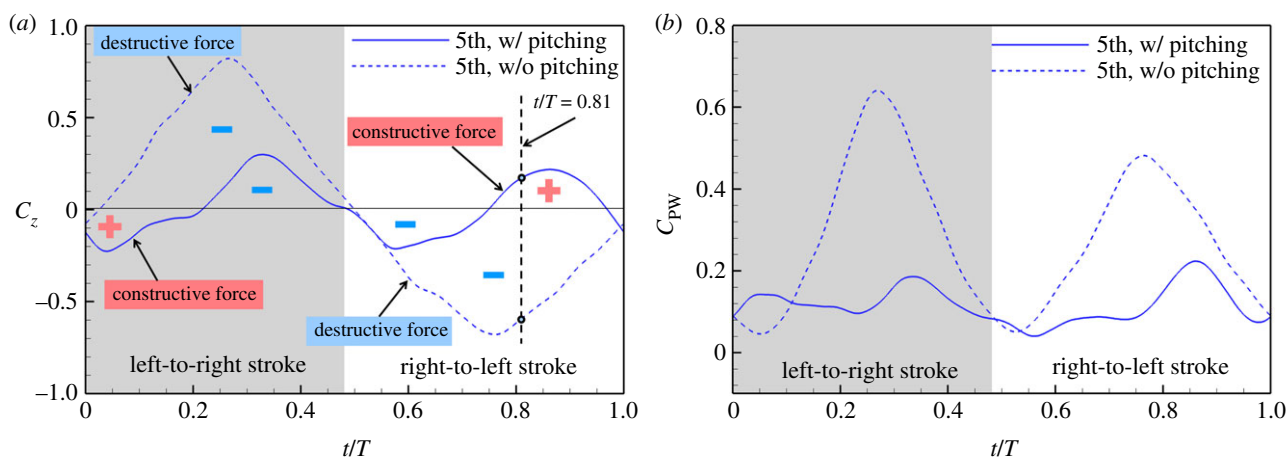


**Figure 12.** Comparisons of instantaneous lateral force coefficients (a) and power coefficients (b), respectively, between the fifth finlet with and without pitching. In (a), the regions between constructive force and  $C_z = 0$  are marked with red plus signs (+) and those between the destructive force and  $C_z = 0$  are marked with blue minus signs (–).

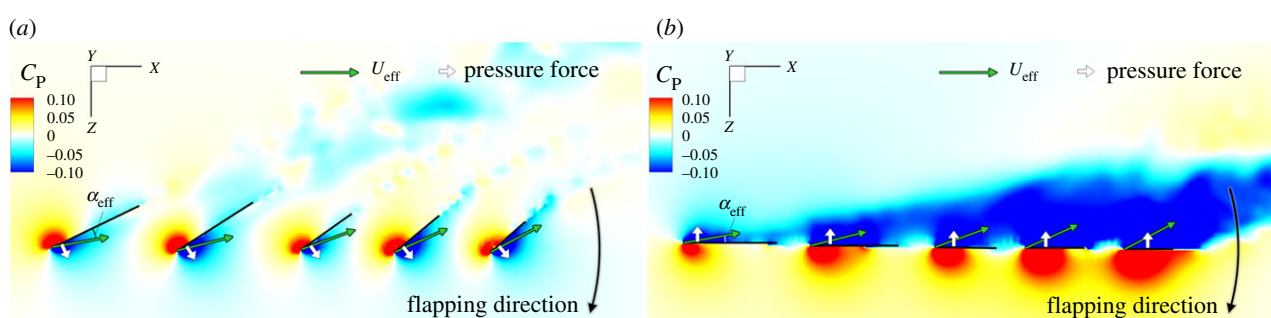


**Figure 13.** Comparisons of the normalized pressure coefficient ( $C_p$ ) contour of the finlets with (a) and without (b) pitching motions, respectively, at  $t/T = 0.81$  on a horizontal slice cutting through a chord of the first finlet.  $\alpha_{\text{eff}}$  denotes the effective angle of attack and  $U_{\text{eff}}$  denotes the effective velocity at the finlet root.

and fifth) was reduced as a result of pitching. Even though the power consumption of the first finlet increased by a large 73% because of its role in generating mean lateral force, the total power consumption of the pitching finlets was still 20.8% less than that of finlets without pitching, which is a beneficial hydrodynamic effect of finlet pitching motion.

It was found that the instantaneous lateral force on pitching finlets could facilitate posterior body flapping (figure 12a). Specifically, the direction of lateral force generated by the pitching fifth finlet was along the negative  $z$ -axis during the first half of the L-to-R stroke, which was in the same direction as the flapping motion of the posterior body of the fish. This could facilitate the oscillation of the fish's posterior body by providing augmented lateral force from the finlet, which we call the constructive force. This same constructive force from the pitching fifth finlet was found during the second half of the R-to-L stroke. However, for the fifth finlet without pitching, the lateral force was always in the opposite direction of posterior body motion for the entire tail beat cycle (figure 12a), which means that the fifth finlet was always generating a destructive force that adds more lateral drag to the posterior body. Moreover, the amplitude of the destructive force of the body-fixed finlet was much larger than that of the pitching finlet, which caused increases in both the mean and the instantaneous power consumption (figures 11b and 12b). Besides the fifth finlet, significant constructive forces were also generated by the fourth finlet during the first half of the L-to-R stroke and the second half of the R-to-L stroke, and by the first and second finlets at the entire R-to-L stroke (figure 10a).

The mechanism of hydrodynamic pressure force production is demonstrated by the instantaneous pressure contour around pitching finlets (figure 13a) at  $t/T = 0.81$ . The  $\alpha_{\text{eff}}$  for all finlets are positive (figure 10c) at that moment, which is in line with the positive  $\alpha_{\text{eff}}$  of the fifth mackerel finlet at a similar tail-flapping phase observed by Nauen & Lauder [6] using flow visualization. As a result, high- and low-pressure zones were formed on the right and the left side of finlets, respectively, producing pressure forces normal to the finlet surfaces pointing to the left (white arrows in figure 13a). As a result of the positive geometric angle of attack ( $\alpha$ ) of finlets, the pressure forces had positive  $x$ -components, which contribute to finlet drag. The positive  $z$ -components of the pressure forces were in the same direction as the posterior body motion, which is the source of constructive forces on finlets at the moment (figure 10a). However, for finlets without pitching kinematics (figure 13b), the  $\alpha_{\text{eff}}$  of finlets were all negative (figure 10c), resulting in pressure force directions being opposite to the flapping direction; therefore, they are destructive for posterior body flapping. Also, the pressure differences between the two sides of body-fixed finlets were much larger than those of the pitching finlets, causing more severe destructive drag on the posterior body during middle R-to-L stroke.

Since finlets are located immediately upstream of the caudal fin, it is important to investigate the effect of pitching kinematics of finlets on the local flow that is incident to the main propulsor of the fish. We found that the flow past pitching finlets was redirected into streams parallel to the orientation of finlets at middle R-to-L stroke ( $t/T = 0.81$ ) (figure 14a). These streams

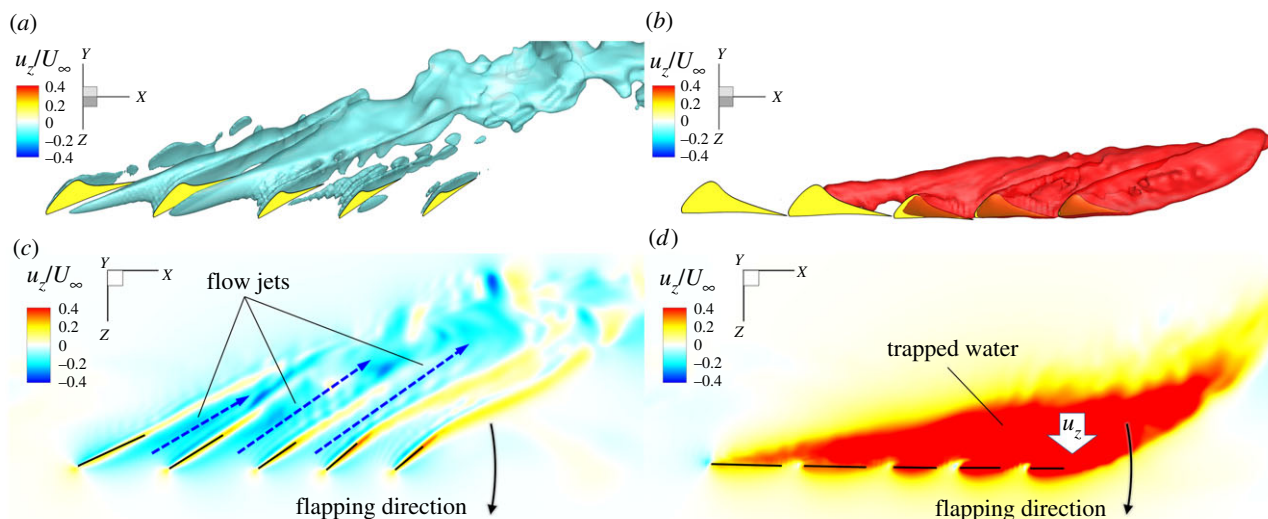


**Figure 14.** Comparisons of the normalized lateral velocity ( $u_z/U_\infty$ ) isosurface (a,b) and contour (c,d) of the finlets with (a,c) and without (b,d) pitching kinematics, respectively, at  $t/T = 0.81$  on a horizontal slice cutting through a chord of the first finlet.

move across the body midline through channels between finlets towards the opposite direction of tail flapping (figure 14c). For finlets without pitching (figure 14b), however, the local flow was trapped and carried away by finlets towards the direction of tail flapping. Significant positive lateral flow velocity (in red, figure 14d) induced by body-fixed finlets was found at the region where the water was trapped. The strong positive lateral flow may explain the much higher power consumption of the last three body-fixed finlets in figure 11b because more work from finlets is required to increase the kinetic energy of trapped water. Additional effects of finlet flows on the caudal fin are presented in the electronic supplementary material.

## 4. Discussion

The flow pattern of pitching finlets in figure 14a,c was in line with the finding by Nauen & Lauder [4] that cross-peduncular flow redirected by finlets exists in the horizontal plane. The current results support the hypotheses of Walters [7], Webb [8] and Lindsey [3] that transverse flow was redirected by the finlets and also support the ‘flow fences’ hypothesis by Magnuson [9] that finlets helped direct the water smoothly across the caudal peduncle. Owing to the absence of a caudal fin, the results above could not directly support the vorticity enhancement hypothesis by Nauen & Lauder [4] on the mackerel, suggesting that finlets can direct flow into the vortex formation at the caudal fin. However, the existence of the redirected flow has provided a potentially favourable local flow environment upstream of the caudal fin and suggests that such caudal vortex enhancement is a distinct possibility. As an extended effort to demonstrate the finlet–caudal fin interaction, we have provided simulation results of tuna full-body swimming in the electronic supplementary material, in which substantial interactions between the finlet-induced vortex and the caudal fin are observed.

Although beneficial interactions that enhance caudal fin thrust have been found between the median and the caudal fins in thunniform [13] and carangiform swimming [16], the fluid dynamics of finlet–caudal fin interactions may be different from other median fins studied previously. Specifically, the simplified finlets and median fin models adopted by previous computational studies [13–16] were strip-like elongated

fins, and not individual distinct and isolated finlets each moving independently. The flow induced by the tip of the simplified strip-like finlets [14] and dorsal/anal fins [16] was generally a cone-shaped vortex tube along the strip with the apex attached to the upstream end, similar to the vortex wake generated by the body-fixed finlets in figure 10e,g. By contrast, the wake topology changed drastically after adding independent pitching kinematics to the individual finlets. Each finlet generated a vortex pair with its orientation deviating from the body midline, creating a matrix of parallel vortex tubes in figure 6e,f. This is a new flow pattern found here for finlet flows, and is distinct from previous computational studies of median fin function [13–16]. These data suggest the potential for novel fluid dynamic interactions between finlet flows and the tail fin in swimming fish, a phenomenon that will be explored in future work.

Limitations on the numerical modelling of this work include the use of uniform incoming flow without a tuna body (although see the electronic supplementary material for simulations that include the body) at a reduced Reynolds number, which has been proven to be valid for the current conclusions (see §2.2 and the electronic supplementary material for further details). The present simulation is representative of yellowfin tuna steady swimming at the speed range of 0.25–0.46 body lengths per tail beat cycle. The main conclusions may not apply to tuna swimming at speeds other than this range or other swimming behaviours (manoeuvre, acceleration/desecration), or for other Scombridae species with finlet morphology distinct from yellowfin tuna.

## 5. Conclusion

In this paper, both anatomically and kinematically accurate finlet models have been reconstructed based on video data from freely swimming yellowfin tuna. Direct numerical simulation results show that finlets were drag producing mainly because of the drag component of the hydrodynamic pressure force, which is determined by both the geometric angle of attack and the effective angle of attack of finlets. The FFI significantly helped to reduce total finlet drag, and the pitching kinematics of finlets helped to reduce finlet power consumption during swimming. Significant mean lateral forces were

generated by the finlets, which may assist in manoeuvring by generating yaw torques. Moreover, the pitching finlets created constructive forces to facilitate posterior body flapping when their effective angles of attack and root  $z$ -velocities have the same sign. Wake dynamics analysis revealed a unique vortex tube matrix structure and the associated flow jets redirected through the channels between pitching finlets, which supports previous hypotheses that finlets can redirect and modulate the transverse flow. These findings suggest that, although pitching finlets do not produce thrust, they have substantially transformed the flow incident to the tail, which may further cause beneficial interactions with the tail fin.

## References

- Yuen HSH. 1970 Behavior of skipjack tuna, *Katsuwonus pelamis*, as determined by tracking with ultrasonic devices. *J. Fish. Res. Board Can.* **27**, 2071–2079. (doi:10.1139/f70-231)
- Beamish FWH. 1978 Swimming capacity. *Fish Physiol.* **7**, 101–187. (doi:10.1016/S1546-5098(08)60164-8)
- Lindsey CC. 1978 Form, function and locomotory habits in fish. *Fish Physiol.* **7**, 1–100. (doi:10.1016/S1546-5098(08)60163-6)
- Nauen JC, Lauder GV. 2000 Locomotion in scombrid fishes: morphology and kinematics of the finlets of the chub mackerel *Scomber japonicus*. *J. Exp. Biol.* **203**, 2247.
- Nauen JC, Lauder GV. 2001 Three-dimensional analysis of finlet kinematics in the chub mackerel (*Scomber japonicus*). *Biol. Bull.* **200**, 9–19. (doi:10.2307/1543081)
- Nauen JC, Lauder GV. 2001 Locomotion in scombrid fishes: visualization of flow around the caudal peduncle and finlets of the chub mackerel *Scomber japonicus*. *J. Exp. Biol.* **204**, 2251.
- Walters V. 1962 Body form and swimming performance in the scombrid fishes. *Am. Zool.* **2**, 143–149. (doi:10.1093/icb/2.2.143)
- Webb PW. 1975 Hydrodynamics and energetics of fish propulsion. *Bullet. Fish. Res. Board Can.* **190**, 1–159.
- Magnuson JJ. 1970 Hydrostatic equilibrium of *Euthynnus affinis*, a pelagic teleost without a gas bladder. *Copeia* **1970**, 56–85. (doi:10.2307/1441976)
- Wardle CS. 1977 Effects of size on the swimming speeds of fish. In *Scale effects in animal locomotion* (ed. TJ Pedley), pp. 299–313. New York, NY: Academic Press.
- Aleev IU. 1969 *Function and gross morphology in fish*. Jerusalem, Israel: Keter Publishing House.
- Helfman G, Collette B, Facey D. 1997 *The diversity of fishes*. Malden, MA: Blackwell Scientific Publications.
- Zhu Q, Wolfgang MJ, Yue DKP, Triantafyllou MS. 2002 Three-dimensional flow structures and vorticity control in fish-like swimming. *J. Fluid Mech.* **468**, 1–28. (doi:10.1017/S002211200200143X)
- Wang S, Zhang X, He G. 2015 Numerical simulation of a three-dimensional fish-like body swimming with finlets. *Commun. Comput. Phys.* **11**, 1323–1333. (doi:10.4208/cicp.090510.150511s)
- Najafi S, Abbaspour M. 2017 Numerical study of propulsion performance in swimming fish using boundary element method. *J. Brazilian Soc. Mech. Sci. Eng.* **39**, 443–455. (doi:10.1007/s40430-016-0613-8)
- Liu G, Ren Y, Dong H, Akanyeti O, Liao JC, Lauder GV. 2017 Computational analysis of vortex dynamics and performance enhancement due to body-fin and fin-fin interactions in fish-like locomotion. *J. Fluid Mech.* **829**, 65–88. (doi:10.1017/jfm.2017.533)
- Wainwright DK, Lauder GV. 2020 Tunas as a high-performance fish platform for inspiring the next generation of autonomous underwater vehicles. *Bioinspir. Biomim.* **15**, 035007. (doi:10.1088/1748-3190/ab75f7)
- Collette BB, Nauen CE. 1983 *FAO species catalogue. Volume 2. Scombrids of the world. An annotated and illustrated catalogue of tunas, mackerels, bonitos and related species known to date*. See <http://www.fao.org/3/ac478e/ac478e00.htm>.
- Koehler C, Liang Z, Gaston Z, Wan H, Dong H. 2012 3D reconstruction and analysis of wing deformation in free-flying dragonflies. *J. Exp. Biol.* **215**, 3018–3027. (doi:10.1242/jeb.069005)
- Liu G, Ren Y, Zhu J, Bart-Smith H, Dong H. 2015 Thrust producing mechanisms in ray-inspired underwater vehicle propulsion. *Theoret. Appl. Mech. Lett.* **5**, 54–57. (doi:10.1016/j.taml.2014.12.004)
- Mittal R, Dong H, Bozkurtas M, Najjar FM, Vargas A, von Loebbecke A. 2008 A versatile sharp interface immersed boundary method for incompressible flows with complex boundaries. *J. Comput. Phys.* **227**, 4825–4852. (doi:10.1016/j.jcp.2008.01.028)
- Fish EF, Schreiber MC, Moored WK, Liu G, Dong H, Bart-Smith H. 2016 Hydrodynamic performance of aquatic flapping: efficiency of underwater flight in the manta. *Aerospace* **3**, 20. (doi:10.3390/aerospace3030020)
- Pavlov V, Rosenthal B, Hansen NF, Beers JM, Parish G, Rowbotham I, Block BA. 2017 Hydraulic control of tuna fins: a role for the lymphatic system in vertebrate locomotion. *Science* **357**, 310–314. (doi:10.1126/science.aak9607)
- Li N, Liu H, Su Y. 2017 Numerical study on the hydrodynamics of thunniform bio-inspired swimming under self-propulsion. *PLoS ONE* **12**, e0174740. (doi:10.1371/journal.pone.0174740)
- Zhu J, White C, Wainwright DK, Di Santo V, Lauder GV, Bart-Smith H. 2019 Tuna robotics: a high-frequency experimental platform exploring the performance space of swimming fishes. *Sci. Robot.* **4**, eaax4615. (doi:10.1126/scirobotics.aax4615)
- Zhong Q, Dong H, Quinn DB. 2019 How dorsal fin sharpness affects swimming speed and economy. *J. Fluid Mech.* **878**, 370–385. (doi:10.1017/jfm.2019.612)
- Dong H, Mittal R, Najjar FM. 2006 Wake topology and hydrodynamic performance of low-aspect-ratio flapping foils. *J. Fluid Mech.* **566**, 309–343. (doi:10.1017/S002211200600190X)
- Bozkurtas M, Mittal R, Dong H, Lauder GV, Madden P. 2009 Low-dimensional models and performance scaling of a highly deformable fish pectoral fin. *J. Fluid Mech.* **631**, 311–342. (doi:10.1017/S0022112009007046)
- Borazjani I, Sotiropoulos F. 2008 Numerical investigation of the hydrodynamics of carangiform swimming in the transitional and inertial flow regimes. *J. Exp. Biol.* **211**, 1541–1558. (doi:10.1242/jeb.015644)
- Hunt JC, Wray AA, Moin P. 1988 Eddies, streams, and convergence zones in turbulent flows. In *Proc. of the 1988 Summer Program Studying Turbulence Using Numerical Simulation Databases, 2*, pp. 193–208. Center for Turbulence Research, NASA, USA. See <https://ntrs.nasa.gov/search.jsp?R=19890015184>.